J. Appl. Comput. Mech., 12(3) (2026) 1276-1287
DOI: 10.22055/jacm.2026.48841.5540

ISSN: 2383-4536
jacm.scu.ac.ir

Shahid Chamran University of Ahvaz

Journal of Applied and Computational Mechanics

Research Paper

# GPU-Accelerated High-Fidelity Simulation of Turbulent Natural Convection

Alexander Nee

Research School of High-Energy Physics, National Research Tomsk Polytechnic University, Tomsk, Russia, Email: nee_alexander@mail.ru

Received October 20 2025; Revised February 06 2026; Accepted for publication April 26 2026.
✉ Corresponding author: A. Nee (nee_alexander@mail.ru)


**Abstract.** This paper presents the hybrid meso-macroscopic model for high-fidelity simulation of turbulent thermal flows. The two-relaxation lattice Boltzmann solver with the fourth order equilibrium distribution function representation was used to compute flow fields. Numerical integration of the energy equation was performed using a fourth-order Runge-Kutta method. In-house MATLAB and Julia codes were developed using CUDA tools. Turbulent natural convection of air was considered in a Rayleigh number range of $10^{10} \le Ra \le 10^{11}$ and aspect ratio range of $0.5 \le A_r \le 2$. It was found that distribution of the second order statistics is mainly determined by convective plumes dynamics. The aspect ratio affects the level of heat stratification. Moreover, the horizontal distribution of temperature variance and turbulent kinetic energy with $Ra = 10^{10}$ is altered to vertical distribution with $Ra = 10^{11}$ when $A_r = 2$. The hybrid lattice Boltzmann scheme predicts the mean Nusselt numbers with error of no more than 1% and 4% when $Ra = 10^{10}$ and $Ra = 10^{11}$, respectively, compared to classical DNS techniques. The model performance achieves 1776 MLUPS and 1048.58 MLUPS with NVIDIA Tesla V100 when using single and double precision variables, respectively. This level of computational performance creates an opportunity for the real-time prediction of thermal turbulence characteristics.

**Keywords:** GPU computing; Thermal turbulence; High-performance computing; Hybrid LBM; Parallel simulation.

## 1. Introduction

Natural convection in an air-filled enclosure with differential sidewalls heating/cooling and thermally-insulated horizontal boundaries is a benchmark CFD problem. Numerous studies are performed in order to better understand heat transfer and fluid flow patterns of thermal convection. Despite a significant progress in numerical theory and computer science, Rayleigh-Benard convection in closed cavities is well studied in a range of Rayleigh number only up to $10^9$. When the buoyancy force is further increased, developed turbulent flow is formed. In this case, the common practice is to utilize the Reynolds averaged Navier-Stokes (RANS) solver [1, 2]. However, this technique contains many empirical constants. Moreover, the RANS was mainly elaborated for forced convection. Thus, RANS models can produce inaccurate results with high Rayleigh numbers. For example, Barakos et al. [3] implemented the standard RANS model of kinetic energy and its dissipation rate $(k-\varepsilon)$ to study natural convective flow in a square cavity. The authors stated that this model even with wall function inaccurately predicted the heat transfer by natural convection with $Ra \geq 10^{10}$. Hence, the large eddy simulation (LES) or the direct numerical simulation (DNS) techniques should be used to study thermal flows. But these approaches are still computationally expensive. The works concerned with the DNS and the LES analysis of buoyancy-driven flows with $Ra \geq 10^{10}$ will be discussed below.

One of the earliest works on the direct numerical simulation of turbulent natural convection was performed by Paolucci [4]. The author wanted to demonstrate that the theories developed for turbulent heat and mass transfer under forced boundary-layer flow were not applicable to buoyancy-driven turbulence. Despite the three-dimensional nature of the turbulent flow, the author stressed that the two-dimensional problem formulation can be used as the first approximation in many cases when thermal stratification was encountered. The high-resolution three-dimensional simulations were performed by Fusegi et al. [5]. The authors proposed the *Nu*-*Ra* correlation in a range of $10^3 \leq Ra \leq 10^{10}$ which is still used for validation of turbulence models.

An important contribution on the DNS for natural convection has been made by Trias et al. [6-9]. The authors studied both weak and fully developed buoyancy-driven flows up to $10^{11}$. The Navier-Stokes equations were discretized by the second and the fourth order explicit schemes. In order to reduce the grid size, a tall air-filled cavity with aspect ratio of 4 was considered. Instantaneous and time-averaged heat transfer and fluid flow patterns were presented and analyzed. It was found that the stratified cavity core and convective cells near the corners were formed in all simulation cases. Later, Trias et al. [9] proposed a regularization procedure of convective terms to reduce the computational costs.

The large eddy simulation is a compromise between accuracy and computational costs. Vasiliev et al. [10] experimentally and numerically studied turbulent natural convection in a cubic cavity with heat-insulated sidewalls. Variation range of governing parameters were $2 \cdot 10^9 \leq Ra \leq 1.6 \cdot 10^{10}$ and $3.5 \leq \Pr \leq 6.1$. It was demonstrated that the Smagorinsky LES-based model within the commercial software ANSYS CFX satisfactorily reproduced turbulent natural convective patterns.

Published online: May 03 2026

**Table 1.** A brief summary on turbulent natural convection simulation performed by other researchers.

| Reference | Problem | Method | *Ra* | Aspect ratio | Grid |
|---|---|---|---|---|---|
| Paolucci [4] | 2D | DNS | $10^{10}$ | 1 | 121×121 |
| Fusegi et al. [5] | 3D | DNS | $10^3 \le Ra \le 10^{10}$ | 1 | 122×62×62 |
| Trias et al. [6, 7] | 3D | DNS | $6.4\times10^8 \le Ra \le 10^{11}$ | 4 | 128×684×1278 |
| Dixit and Babu [13] | 2D | BGK LBM | $10^4 \le Ra \le 10^{10}$ | 1 | 512×512 |
| Sharma et al. [14] | 2D | Cascaded LBM | $10^6 \le Ra \le 10^{10}$ | 1 | 2048×2048 |
| Frapolli et al. [15] | 3D | Entropic LBM | $10^7 \le Ra \le 10^{11}$ | 0.5 | 384×384×768 |
| Wen et al. [17] | 3D | DUGKS | $1.5\times10^9 \le Ra \le 10^{11}$ | 1 | 320×320×320 |

The higher Rayleigh number flows were analyzed by Sondak et al. [11] in terms of the WALE model. An impressive range of $10^6 \le Ra \le 10^{14}$ was considered using the finite element Drekar code. Performance of different SGS models was analyzed by Kizildag et al. [12] in terms of a water-filled tall cavity with $Ra = 3\cdot 10^{11}$. As the benchmark data were used DNS results. It was revealed that the VMS-WALE and WALE models better predicted overall flow behavior than the QR model.

The turbulent flow can also be simulated by an alternative CFD technique called the lattice Boltzmann method. In this case, mesoscopic equations for distribution function are solved in order to obtain macroscopic characteristics of flow. Dixit and Babu [13] studied both laminar and turbulent natural convection in a closed square cavity with isothermal sidewalls. To make the wide-spread BGK approximation numerically stable with high Rayleigh numbers up to $10^{10}$, the authors performed an interpolation procedure. The same range of the Rayleigh number was considered in Sharma et al. [14]. Tehy implemented the cascaded approximation scheme of collision operator in the Boltzmann equation. The higher values of buoyancy force were examined by Frapolli et al. [15]. The authors implemented the double population entropic lattice Boltzmann model. Fully-developed turbulent buoyancy-driven flow under non-rotating and rotating conditions was studied.

Direct numerical simulation of turbulent natural convection in terms of the discrete unified gas-kinetic scheme (DUGKS) was performed in [16, 17]. A wide range of $10^3 \le Ra \le 10^{11}$ was analyzed and the laminar-to-turbulent transition inside the boundary layers at the isothermal walls was discussed.

It needs to be stressed that the LES can be easily implemented within the LBM since the strain-rate tensor can be derived through the non-equilibrium distribution function. Zhuo and Zhong [18] proposed a novel LES based thermal filter-matrix lattice Boltzmann model. In order to accurately simulate the near-wall region, the Vreman SGS model was implemented. Turbulent natural convection with double diffusion in a square cavity was examined by Chen et al. [19]. Heat and mass transfer was analyzed with *Ra* up to $10^{11}$. Table 1 presents a brief summary on turbulent natural convection simulation performed by other researchers.

To summarize the results of literature review, it was found that only few papers discussed highly turbulent natural convection with $Ra = 10^{11}$. On the one hand, this can be explained by significant computational costs. On the other hand, numerical procedure gets much more complicated and becomes a great challenge for many researchers when implementing high order approximation schemes. Indeed, the lattice Boltzmann method can resolve the first issue due to high level of parallelism. However, it is well-known that simple LBGK model is unstable with high Reynolds or Rayleigh numbers. To overcome this weakness, advanced approximations of collision operator such as the entropic and cascaded MRT are implemented. And again, numerical procedure becomes very complicated. The motivation of the present work is to build a simple and robust model for highly turbulent buoyancy-driven flows. For this purpose, the mesoscopic lattice Boltzmann equation for flow will be coupled with macroscopic energy equation for temperature. This hybrid link provides higher numerical stability as was reported in [20]. To further increase numerical stability, collision operator will be approximated by the two-relaxation time (TRT) scheme. This approximation scheme is as simple as the BGK in terms of the numerical implementation. Note that, previously, the laminar models [21, 22] were proposed and under-resolved turbulence simulation [23] was performed. In this study, the high-fidelity simulation is discussed using the hybrid lattice TRT model supplemented with the fourth order representation of the equilibrium distribution function.

## 2. Problem Formulation

As stated by Paolucci [4], two-dimensional model can be used as the first approximation when analyzing turbulent buoyancy-driven flows. The 2D simulation significantly reduces computational costs. Hence, the grid can be fine enough to resolve small eddies whereas execution time of the code will be acceptable. In order to make numerical procedure easier, isotropic turbulence is considered. Along with that, dependence of physical properties on the temperature is neglected. Cavity configuration is typical (Fig. 1). Horizontal boundaries are perfectly insulated whereas the Dirichlet conditions are set at the vertical walls.

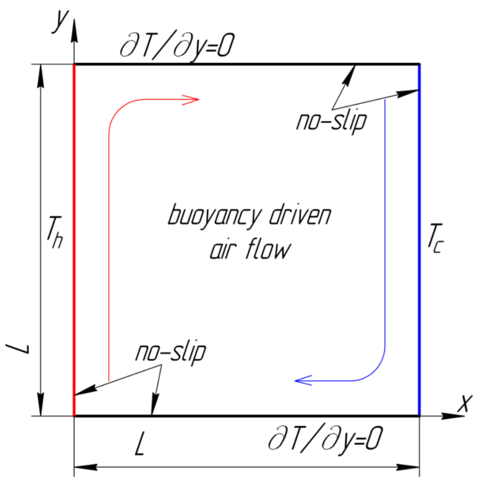


**Fig. 1.** Geometrical model.

Within the direct numerical simulation technique, the turbulent fluid flow is described by Navier-Stokes equations as follows:

$$\rho\left(\frac{\partial u}{\partial t}+u\frac{\partial u}{\partial x}+v\frac{\partial u}{\partial y}\right)=-\frac{\partial p}{\partial x}+\mu\left(\frac{\partial^2 u}{\partial x^2}+\frac{\partial^2 u}{\partial y^2}\right), \tag{1}$$

$$\rho\left(\frac{\partial v}{\partial t}+u\frac{\partial v}{\partial x}+v\frac{\partial v}{\partial y}\right)=-\frac{\partial p}{\partial y}+\mu\left(\frac{\partial^2 u}{\partial x^2}+\frac{\partial^2 v}{\partial y^2}\right)+\rho\cdot g\cdot\beta_T\cdot(T-T_0), \tag{2}$$

$$\frac{\partial u}{\partial x}+\frac{\partial v}{\partial y}=0, \tag{3}$$

The lattice Boltzmann equations approximated by the two-relaxation time scheme are applied to reproduce macroscopic fluid flow characteristics. The discretized form of the governing equations is as follows [24]:

$$f_k\left(\vec{x}+\vec{c}_k\cdot\Delta t, t+\Delta t\right)=f_k\left(\vec{x}, t\right)-\frac{\Delta t}{\tau_{sym}}\cdot\left(f_k^{sym}-f_k^{seq}\right)-\frac{\Delta t}{\tau_{asym}}\cdot\left(f_k^{asym}-f_k^{aeq}\right)+\Delta t\cdot c_k\cdot F_k. \tag{4}$$

The symmetrical $\tau_{sym}$ and asymmetrical $\tau_{asym}$ relaxation times, symmetrical $f_k^{sym}$ and asymmetrical $f_k^{asym}$ distribution functions, symmetrical $f_k^{seq}$ and asymmetrical $f_k^{aeq}$ equilibrium distribution functions, force, density and velocity are given by:

$$\tau_{sym}=\frac{\nu_{lb}}{c_s^2\cdot\Delta t}+\frac{1}{2}. \tag{5}$$

$$\tau_{asym}=\frac{0.5\cdot\tau_{sym}}{\tau_{sym}-0.5}. \tag{6}$$

$$f_k^{sym}=\frac{f_k+f_{-k}}{2}. \tag{7}$$

$$f_k^{seq}=\frac{f_k^{eq}+f_{-k}^{eq}}{2}. \tag{8}$$

$$f_k^{asym}=\frac{f_k-f_{-k}}{2}. \tag{9}$$

$$f_k^{aeq}=\frac{f_k^{eq}-f_{-k}^{eq}}{2}. \tag{10}$$

$$F_k=w_k\cdot\frac{\rho\cdot g\cdot\beta\cdot(T-T_0)}{c_s^2}. \tag{11}$$

$$\rho=\sum_{k=1}^{19}f_k. \tag{12}$$

$$u=\frac{1}{\rho}\cdot\sum_{k=1}^{19}c_k\cdot f_k. \tag{13}$$

In the above equations, the subscript "–*k*" denotes the opposite direction of the subscript "*k*" (Fig. 2). Note that the high order equilibrium distribution function representation is used to better resolve turbulent structures:

$$f_k^{eq}=w_k\cdot\rho\cdot\left[1+\frac{c_k\cdot\mathbf{u}}{c_s^2}+\frac{(c_k\cdot\mathbf{u})^2}{2\cdot c_s^4}-\frac{\mathbf{u}^2}{2\cdot c_s^2}+\frac{(c_k\cdot\mathbf{u})^3}{6\cdot c_s^6}-\frac{(c_k\cdot\mathbf{u})\mathbf{u}^2}{2\cdot c_s^4}+\frac{(c_k\cdot\mathbf{u})^4}{24\cdot c_s^8}-\frac{(c_k\cdot\mathbf{u})^2\mathbf{u}^2}{4\cdot c_s^6}+\frac{\mathbf{u}^4}{8\cdot c_s^4}\right]. \tag{14}$$

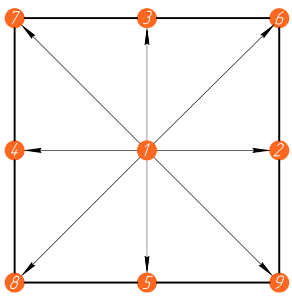


**Fig. 2.** The D2Q9 scheme.

To improve the algorithm numerical stability, the energy equation is directly solved by means of the conventional finite difference method. Lallemand and Luo [20] proved that this hybrid lattice Boltzmann formulation [25] increases stability. The governing equation is as follows:

$$\frac{\partial T}{\partial t}+u\frac{\partial T}{\partial x}+v\frac{\partial T}{\partial y}=a\left(\frac{\partial^2 T}{\partial x^2}+\frac{\partial^2 T}{\partial y^2}\right). \tag{15}$$

The second order partial differential equation (7) is closed by the following initial and boundary conditions:

$$t=0,\ T=T_0. \tag{16}$$

$$t>0,\ x=0,\ 0<y<L,\ T=T_h. \tag{17}$$

$$t>0,\ x=L,\ 0<y<L,\ T=T_c. \tag{18}$$

$$t>0,\ y=0,\ 0<x<L,\ \frac{\partial T}{\partial y}=0. \tag{19}$$

$$t>0,\ y=L,\ 0<x<L,\ \frac{\partial T}{\partial y}=0. \tag{20}$$

### 2.1. Numerical procedure

It is well-known that the direct numerical simulation is not applied in the modeling of real engineering systems due to enormous computational costs. However, this weakness can be overcome by using a parallel implementation on graphics processing units. In the present study, an in-house parallel code is written in MatLab. The main computations were performed on the MSI ARMOR GTX 1060 6 GB. It needs to be stressed that MatLab is chosen due to its algorithm simplicity when using the parallel computing toolbox. There is no need to work with threads, memory sharing, GPU architecture, etc. as in the case of CUDA/C++ languages. Hence, numerical procedure becomes much more simplified.

The following steps were performed when numerically implementing the hybrid lattice Boltzmann code proposed in this study:

- Initial data input. Firstly, initial numerical data such as grid size, the Rayleigh number, initial conditions, etc. need to be specified. In order to run the code on a graphics processing unit, an array stored on GPU must be created. The command is as follows:

```
T = zeros(Nx,Ny,'gpuArray');
```

Note that the default data type in MatLab is double. However, the data type with single precision consumes twice less memory and is acceptable in many cases:

```
T = single(zeros(Nx,Ny,'gpuArray'));
```

- Start the time or iteration loop. The main steps such as energy equation solution, collision, streaming and macroscopic parameters recovery are performed inside this loop.
- Solve the energy equation. The parabolic partial differential equation of the second order is solved by the fourth order Runge-Kutta technique.
- Collide. Collision step is performed in accordance with Eq. (4).
- Streaming. Propagation step in accordance with two left terms of Eq. (4).
- Boundary conditions. A bounce-back hypothesis is used to find the values of distribution functions at the solid walls.
- Macroscopic parameters recovery. Macroscopic density and velocity are computed in accordance with Eqs. (12) and (13).
- Check the convergence. When $Ra \le 10^8$, a steady-state solution can be reached. In order to find it, the following conditions are set:

$$\left|\Theta^{n+1}-\Theta^{n}\right|<\delta,$$

$$\left|\left(\sqrt{U^2+V^2}\right)^{n+1}-\left(\sqrt{U^2+V^2}\right)^{n}\right|<\delta.$$

- Close the loop.

It needs to be noted that the code should be vectorized in order to achieve the best numerical performance. Ideally, no indices should be used. In this case, the "arrayfun" function can be implemented. This function provides an additional speed-up. For example, the collision step is computationally heavy in the present study. Therefore, this step is written without indices and the "arrayfun" function is implemented as:

```
[f] = arrayfun(@collide, f, U, V, rho, T);
```

To summarize the above, the GPU code is almost identical to the CPU code. The only difference is in the GPU array creation. No more special treatment is needed when running the code on GPU in MatLab. The main loop can be represented as follows:

```
for iter = 1:timesteps
[T] = energy(T);
[f1, f2, f3, f4, f5, f6, f7, f8, f9] = arrayfun(@collision, f1, f2, f3, f4, f5, f6, f7, f8, f9);
[f2, f3, f4, f5, f6, f7, f8, f9] = stream(f2, f3, f4, f5, f6, f7, f8, f9);
[f2, f3, f4, f5, f6, f7, f8, f9] = BC(f2, f3, f4, f5, f6, f7, f8, f9);
[U,V,rho] = arrayfun(@MPR, f1, f2, f3, f4, f5, f6, f7, f8, f9);
end
```

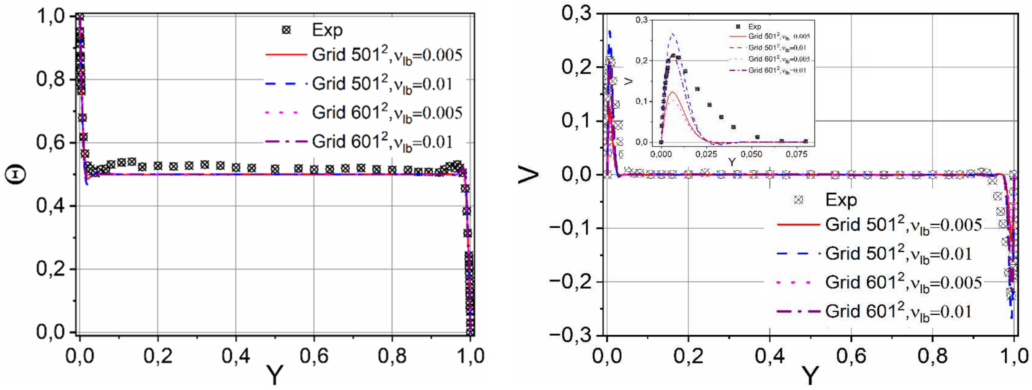


(a) (b)

**Fig. 3.** Temperature (a) and velocity (b) profiles with $Ra$ = 1.58×10$^9$ and Pr = 0.71.

### 2.2. Validation and grid size

Simulation of high Rayleigh number flows by the lattice Boltzmann method is still a challenge. Besides the accuracy, the LBM struggles numerical instabilities with $Ra > 10^9$. In some cases, the lattice viscosity can be decreased in order to maintain algorithm stability. However, this might lead to significant errors during turbulence simulation. Thus, a careful examination of the LBM models for turbulence is of paramount importance. By now, one of the trustful works dealing with buoyancy turbulence is experimental study of Ampofo and Karayiannis [26]. The authors studied turbulent natural convection in a closed rectangular box. Figure 3 presents temperature and velocity variations with lattice viscosity.

During numerical experiments, it was found that the grid size of 501$^2$ ensures numerical stability when the lattice viscosity is set to 0.01. On the contrary, the algorithm is stable with 401$^2$ mesh points when decreasing the $\nu_{lb}$ to 0.005. Figure 3(a) reports identical temperature values when varying the grid size and lattice viscosity. However, a notable deviation in velocity component is found in Fig. 3(b). When $\nu_{lb} = 0.005$, the model underpredicts extremum value both at 501$^2$ and 601$^2$. The maximum velocity value is accurately predicted with $\nu_{lb} = 0.01$ and the grid size of 601$^2$. Note that the deviation in $V$ near the wall is probably due to 2D problem formulation. In general, the hybrid model satisfactory predicts temperature and velocity values.

In order to resolve all relevant convective structures, a very fine mesh should be used. In particular, the high-fidelity simulation of thermal turbulence assumes an accurate resolution of Kolmogorov scales. The dimensionless dissipation scale $(\eta / L)$, Taylor micro-scale $(\lambda / L)$ and thermal boundary layer thickness $(\delta_T / L)$ [15, 27] along with the Rayleigh numbers, aspect ratio $(A_r)$ and grid parameters are given in Table 2. Table 2 indicates that the grid size used in this study ensures accurate resolution of turbulent scales.

## 3. Results and Discussion

The buoyancy-driven flow in a range of $10^4 \le Ra \le 10^9$ has already been studied in detail by other researchers. Hence, turbulent natural convection of air with $10^{10} \le Ra \le 10^{11}$ and Pr = 0.71 is considered in the present study. Heat and fluid flow was considered in terms of the horizontal, square and tall cavities. Numerical simulation results are presented in dimensionless form which is more convenient for overall analysis. The following expressions were used to perform non-dimensionalization procedure:

$$X = \frac{x}{L};\ Y = \frac{y}{L};\quad U = \frac{u}{V_{nc}};\quad V = \frac{v}{V_{nc}};\quad \Theta = \frac{T - T_c}{T_h - T_c};\quad \tau = \frac{t}{t_0};\quad t_0 = \frac{L}{V_{nc}};\quad V_{nc} = \sqrt{g \cdot \beta \cdot (T_h - T_c) \cdot L}.$$

The transient behavior of turbulent natural convection is analyzed in terms of the thermal fields, stream functions, the second order statistics and mean Nusselt numbers. Both instantaneous and time-averaged data are presented. The dimensionless temperature of the left wall is 0.5 whereas the right boundary is kept at -0.5. The isotherms step is 0.05 at the time-averaged plots. Note that the time-averaged values are computed as follows:

$$\overline{T} = \frac{1}{t - t_0} \int_{t_0}^{t} T(x, y, t)\,dt.$$

The start time $(t_0)$ for averaging is shifted to exclude the initial laminar and transition-to-turbulence regimes from the time-averaging procedure. An averaging duration of $8 \cdot 10^5$ and $1.5 \cdot 10^6$ time steps is employed to ensure statistical convergence when $Ra = 10^{10}$ and $Ra = 10^{11}$, respectively.

### 3.1. Temperature and flow

Figure 4 shows thermal fields when varying the aspect ratio. The data is given for $1.5 \cdot 10^6$ iterations. Figure 4 indicates a strong stratified flow inside a horizontal cavity. Despite a turbulent flow behavior, thermal irregularities are only found at the top left and bottom right corners. The reduced height enhances horizontal flow which promotes more uniform temperature gradients. When incrementing the aspect ratio of the cavity, the flow instability is drastically increased. Plumes dynamics is significantly intensified which destratifies thermal field in up-ward and down-ward flow directions. This results in better mixing of the fluid near the isothermal walls. Nevertheless, the central region of the cavity remains thermally stratified.

**Table 2.** Simulation parameters.

| $Ra$ | $N_x$ | $N_y$ | $A_r$ | Δx, Δy/L | $\eta$/L | $\lambda$/L | $\delta_T$/L |
|---|---|---|---|---|---|---|---|
| $10^{10}$ | 801 | 1601 | 2 | 0.000625 | 0.00082 | 0.04 | 0.0045 |
| $10^{11}$ | 2601 | 5201 | 2 | 0.000019 | 0.0004 | 0.0271 | 0.0021 |

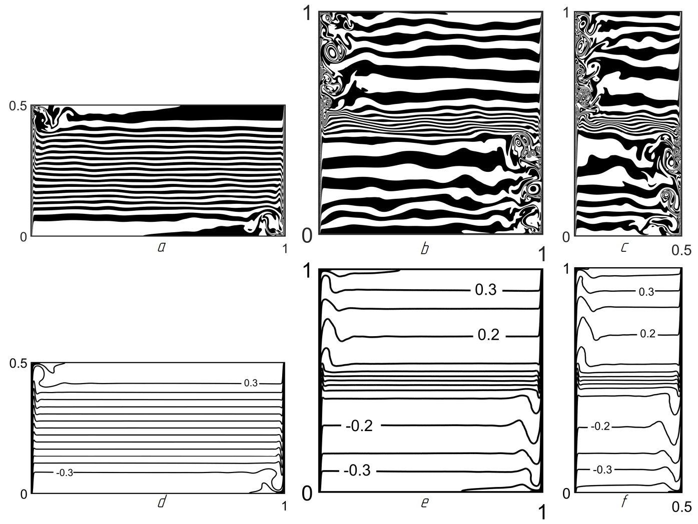


**Fig. 4.** Instantaneous (a, b, c) and time-averaged (d, e, f) temperature contours with $Ra = 10^{10}$: (a, d) $A_r = 0.5$, (b, e) $A_r = 1$, (c, f) $A_r = 2$.

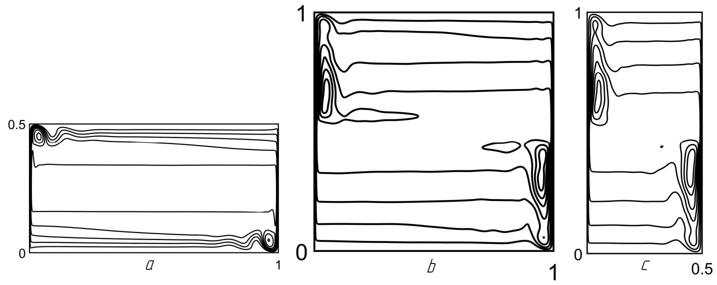


**Fig. 5.** The time-averaged stream function contours with $Ra = 10^{10}$: (a) $A_r = 0.5$, (b) $A_r = 1$, (c) $A_r = 2$.

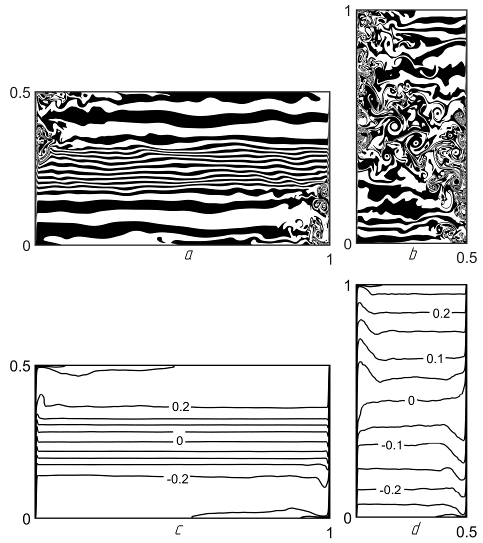


**Fig. 6.** Instantaneous (a, b) and time-averaged (c, d) temperature contours with $Ra = 10^{11}$: (a, c) $A_r = 0.5$, (b, d) $A_r = 2$.

In general, the heat patterns are very similar with $A_r = 1$ and $A_r = 2$. The same level of thermal stratification is observed. Moreover, the detachment area of thermal plumes at the isothermal walls is found almost identical. The time-averaged data indicates a uniform temperature distribution in the horizontal cavity. On the contrary, isotherms in a range of $-0.15 \leq \Theta \leq 0.15$ are concentrated at the cavity core when $A_r = 1$ and $A_r = 2$. Moreover, temperature isolines have identical configuration. It interesting to note that the tall cavity exhibits the lowest/highest temperature values near the top/bottom horizontal walls. This indicates stronger buoyancy effects in the case of $A_r = 2$. The time-averaged flow patterns are given in Fig. 5.

In general, the global flow structure is similar when varying the aspect ratio of the cavity. However, the $A_r$ affects the configuration and location of secondary flows. In particular, thermal plumes determines the shape of inner flows. When $A_r = 0.5$, the areas with secondary flows are only observed at the corners. Notable that outer flows are formed even after time-averaging procedure. However, the size of these areas is insignificant. This results in uniform temperature distribution. On the contrary, the secondary vortices only exist near the isothermal walls with $A_r = 1$. Plumes detachment along with considerable vertical flow influence creates this characteristic pattern. When considering the turbulent natural convection in the tall cavity, the time-averaged flow patter is very similar to the case of $A_r = 1$.

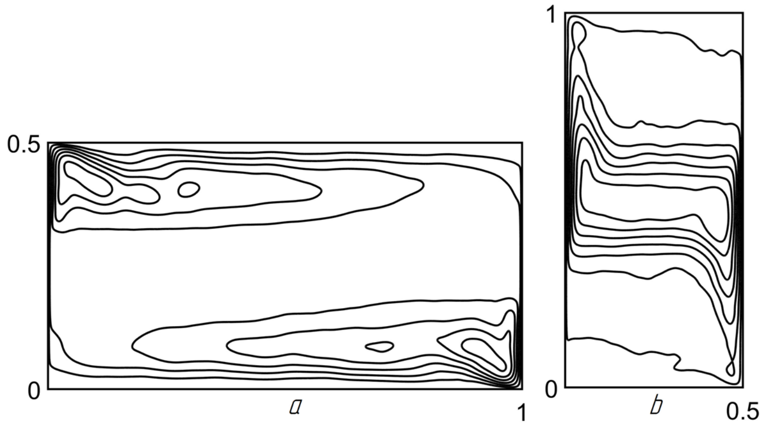


**Fig. 7.** The time-averaged stream function contours with $Ra = 10^{11}$: (a) $A_r = 0.5$, (b) $A_r = 2$.

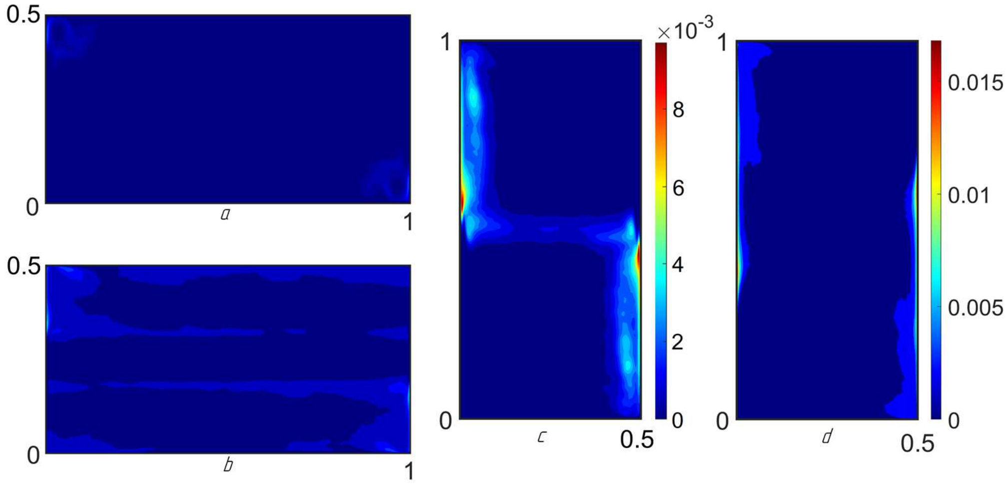


**Fig. 8.** Temperature variance contours when $Ra = 10^{10}$ (a, b) and $Ra = 10^{11}$ (c, d) with (a, c) $A_r = 0.5$, (b, d) $A_r = 2$.

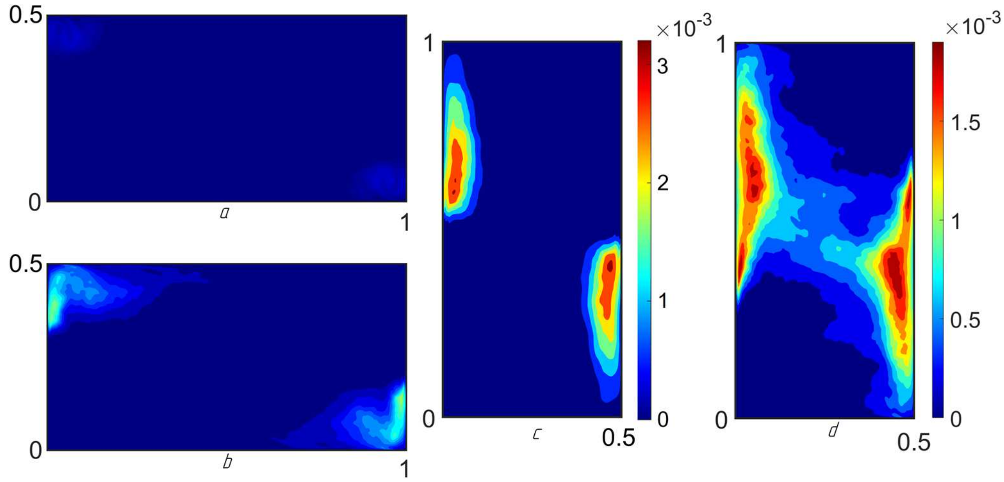


**Fig. 9.** Turbulent kinetic energy contours when $Ra = 10^{10}$ (a, b) and $Ra = 10^{11}$ (c, d) with (a, c) $A_r = 0.5$, (b, d) $A_r = 2$.

However, more uniform stream function isolines are observed along the adiabatic boundaries due to insignificant contribution of horizontal flow. Thermal fields at large Rayleigh number is shown in Fig. 6. Note that the square cavity case is not given due to GPU memory issues.

Despite a strong buoyancy force, the thermal field is remained stratified in the core of the horizontal cavity. Thermal plumes detach in the upstream direction at the isothermal walls and travel along these boundaries. However, the turbulent plumes reach only the top left and bottom right corners. Hereafter, turbulent intensity is decreased and thermal field returns to stratified state. The tall cavity exhibits an inverse thermal pattern. The high rate of plumes production at the isothermal walls destratifies the flow in the core of the cavity. Enhanced plume generation at the isothermal walls disrupts core stratification inducing vigorous fluid mixing in the cavity center. Nevertheless, persistent stratified regions remain evident in the bottom left and top right corners. The time-averaged results reveal marginally higher/lower temperature values near the horizontal boundaries in the tall cavity configuration. Notably, the strong buoyancy effects results in isotherm curvature even after time-averaging procedure. Flow structure is given in Fig. 7.

As anticipated, the internal flow structure within the primary circulation cell undergoes modification with increasing the Rayleigh number. As in the previous case with $Ra = 10^{10}$, the location of the secondary flows is determined by the thermal plumes configuration. When $A_r = 0.5$, the inner convective cells are stretched in the clock-wise direction along the isothermal boundaries. Concurrently, the horizontal cavity core exhibits negligible flow activity. This behavior induces stable thermal stratification in this region. In the tall cavity configuration, secondary flows are observed throughout the entire domain. However, the inner convective cells are placed along the isothermal walls due to the dominance of the vertical flow.

### 3.2. The second order statistics

The temperature variance is given in Fig. 8. Figure 8 shows the intensity of temperature fluctuations in horizontal and tall cavities. When $A_r = 2$, the temperature variance patterns are well predicted by thermal plumes dynamics. Tall cavity case demonstrates predominance of vertical flow near the isothermal boundaries. The area of temperature fluctuations is increased as the Ra is incremented. The different pattern is found in the case of $A_r = 0.5$. The temperature variance is significant along the adiabatic walls with $Ra = 10^{10}$. This indicated the predominance of horizontal flow. However, the pattern is completely changed when $Ra = 10^{10}$. In this case, the vertical flow becomes more significant than the horizontal flow. Nevertheless, the temperature variance is still observed near the adiabatic walls. The turbulent kinetic energy is given in Fig. 9.

Figure 9 presents distributions of turbulent kinetic energy (TKE) when varying the cavity aspect ratio and Rayleigh number. Thermal plumes configuration governs the TKE intensity and spatial organization. In the case of the horizontal cavity, the turbulent kinetic energy concentrates at the corners when $Ra = 10^{10}$. Moreover, the TKE is trying to travel along the adiabatic walls. This indicates the predominance of horizontal flow. The opposite pattern is found when increasing the Rayleigh number. The turbulent kinetic energy is only distributed along the isothermal walls when $A_r = 0.5$ and $Ra = 10^{11}$. The strong buoyancy force forms vertically-dominated thermal plumes dynamics despite the two times higher flow path in the horizontal direction. The tall cavity configuration indicates predominance of vertical flow. Turbulent kinetic energy spreads along the half part of the isothermal walls in clockwise direction with $Ra = 10^{10}$. The locations of the TKE maximum correspond to the initiation points of thermal plumes. When $Ra = 10^{11}$, the area of turbulent kinetic energy distribution is drastically expanded. Thermal plumes travel to the core of the enclosure increasing the TKE. Thermal plumes travel to the core of the enclosure increasing the TKE. The diagonal components of Reynolds stresses $(\sqrt{u'^2}, \sqrt{v'^2})$ are given in Fig. 10.

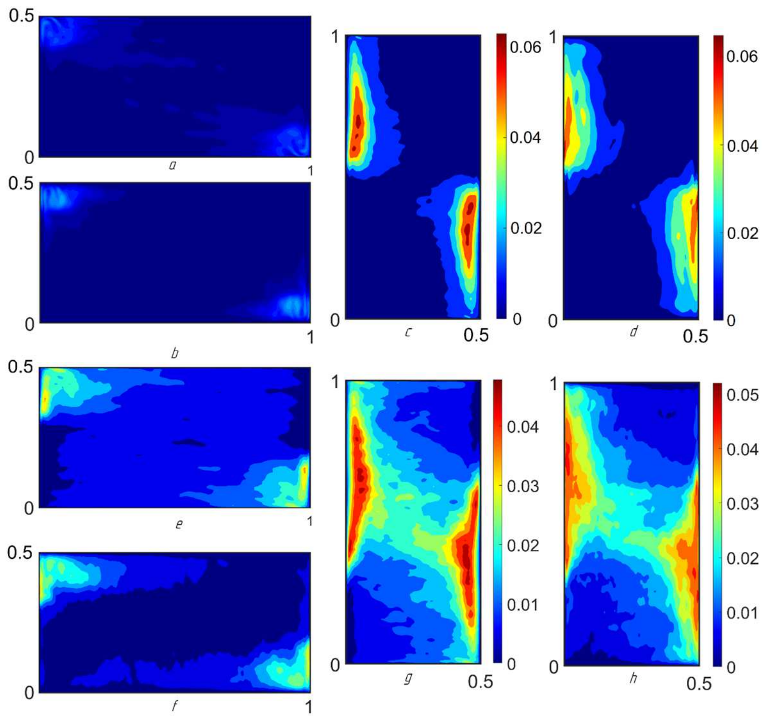


**Fig. 10.** Horizontal (a, c, e, g) and vertical (b, d, f, h) components of Reynolds stresses when $Ra = 10^{10}$ (a, b, c, d) and $Ra = 10^{11}$ (e, f, g, h).

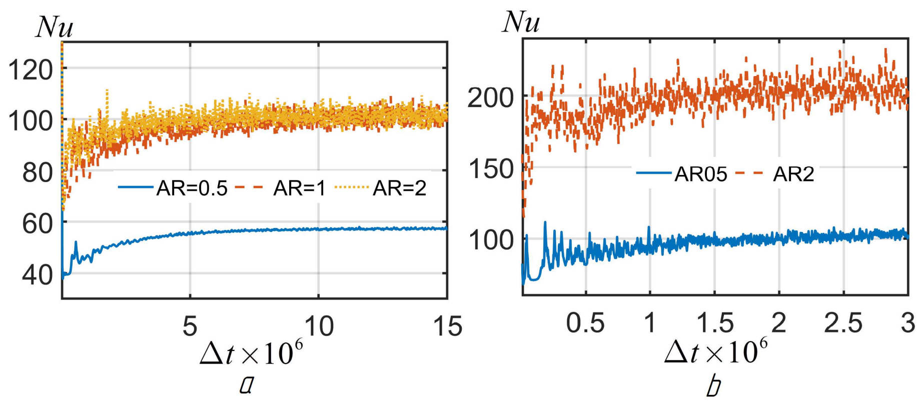


**Fig. 11.** Evolution of mean Nusselt numbers when (a) $Ra = 10^{10}$ and (b) $Ra = 10^{11}$.

**Table 3.** The time-averaged mean Nusselt numbers.

| $Ra$ | $A_r$ = 4, 2D [28] | $A_r$ = 1, 2D [14] | $A_r$ = 1, 3D [17] | $A_r$ = 4, 3D [6] | This study | | | | | |
|---|---|---|---|---|---|---|---|---|---|---|
| | | | | | $A_r$ = 0.5 | | $A_r$ = 1 | | $A_r$ = 2 | |
| | | | | | Float32 | Float64 | Float32 | Float64 | Float32 | Float64 |
| $10^{10}$ | 100.60 | 99.84 | 94.21 | 101.94 | 57.08 | 57.07 | 99.90 | 100.01 | 100.81 | 101.05 |
| $10^{11}$ | - | - | 154.6 | 194.48 | - | 99.71 | - | - | - | 201.94 |

**Table 4.** GPU description.

| GPU | CUDA cores | Memory size | Memory bus width, bit | Memory bandwidth, GB/s |
|---|---|---|---|---|
| Tesla P100 | 3584 | 16 GB of HBM2 | 4096 | 732 |
| Tesla T4 | 2560 | 16 GB of GDDR6 | 256 | 320 |
| Tesla V100 | 5120 | 16 GB of HBM2 | 4096 | 898 |

The spatial distribution of diagonal components of Reynolds stresses is intrinsically governed by the dynamics of thermal plume generation, detachment, and interaction. The same pattern was observed at the turbulent kinetic energy fields. Predictable, the cavity aspect ratio dictates the orientation and organization of fluctuating motions. In the case of the tall cavity, the constrained width promotes strong vertical convection. High-intensity diagonal stresses are generated by buoyant plumes detaching from the vertical walls. As plumes accelerate along the isothermal walls after impingement, the rapid vertical mixing is observed. In the case of the horizontal cavity, diagonal components of Reynolds stresses travel along the adiabatic boundaries. When $Ra = 10^{10}$, the laminar and turbulent regions coexist in both cavity configurations under study. However, flow fluctuations are significantly stronger with $A_r = 2$. Moreover, the fluid is mixed all over the domain when increasing the Rayleigh number to $10^{11}$. The flow fluctuations travel to the core of the tall cavity. On the contrary, the Reynolds stresses are predominantly observed at the top left and bottom right corners when $A_r = 0.5$. Hence, the core of the horizontal cavity remains laminar even with $Ra = 10^{11}$.

### 3.3. Heat transfer rate

The mean heat transfer analysis was performed in terms of the integral Nusselt numbers (*Nu*) computed for the hot isothermal wall. Fig. 11 illustrates the dynamics of mean Nusselt numbers. Note that the time is given in lattice units.

The horizontal cavity case indicates the lowest mean Nusselt number values both at $Ra = 10^{10}$ and $Ra = 10^{11}$. The shorter length of the isothermal walls prevents a full development of the boundary layer. This results in its higher thickness and thermal resistance plays an important role in integral heat transfer. Moreover, it reduces thermal plume generation due to the shorter buoyancy-driven flow path. Consequently, the mean Nusselt number has a moderate oscillation behavior with $A_r = 0.5$. The square cavity configuration gives almost a two-times increase in the Nu in comparison with the horizontal cavity case. This enhancement is obviously due to a longer range of the vertical walls. A decrease in boundary layer thickness creates a steeper temperature gradient at the isothermal walls. The decreased boundary layer thickness results in a steeper temperature gradient at the isothermal walls, thereby increasing the heat transfer rate. Moreover, the longer range of the vertical boundaries intensifies the plume dynamics with high-rate shedding. The tall cavity case gives slightly higher values of the mean Nusselt numbers. Despite an equal size of the vertical walls, a decrease in the cavity length leads to an interaction of the buoyancy-driven flows formed at the isothermal walls. This enhances turbulent mixing throughout the fluid and insignificantly increases the magnitude of Nu oscillations. The time-averaged mean Nusselt numbers are given in Table 3 for validation purposes.

In general, the mean Nusselt number predicted by the high-fidelity TRT LB model is well agreed with reference DNS data. However, a crucial divergence is found when comparing the results with the DUGKS [17]. Probably, this scheme underestimates the heat transfer rate due to excessive numerical dissipation or underresolution of turbulent scales. When $Ra = 10^{10}$ and $A_r \geq 1$, the error is within around 1% both for reliable 2D and 3D DNS models. The large Ra case indicates the deviation of around 4 %. However, TRT LB model utilizes the grid of $2601 \times 5201$ whereas Trias et al. [6] used $128 \times 682 \times 1278$. Hence, a more accurate resolution of turbulent scales due to 2D restriction is given in the present work.

### 3.4. Performance

The implementation of the MATLAB GPU code is simple, yet its performance is not optimal. In contrast, low-level, high-performance CUDA C code is considerably more complex to develop and manage. The high-level Julia language [29], together with the ParallelStencil.jl package [30], offers a unique combination of MATLAB-like simplicity and CUDA C-like performance. The main computation loop is very similar to MATLAB:

```
for iter = 1 : timesteps
@parallel collision!(f1,f2,f3,f4,f5,f6,f7,f8,f9, U,V,rho,T,omega_s,omega_a,feq1, feq2,feq3,feq4,feq5,feq6,feq7,feq8,feq9)
@parallel stream_BC_MPR_energy!(f1, f2, f3, f4, f5, f6, f7, f8, f9, U, V, rho, T)
end
```

The ParallelStencil.jl package enables computational optimization within custom Julia CUDA kernels without the necessity for manual low-level code alterations. Numerical experiments were conducted on different GPUs. Their specification is given in Table 4.

The million lattice update per second (MLUPS) is the standard metric for estimating the numerical performance of the lattice Boltzmann method. It is definition is as follows:

$$MLUPS = \frac{N_x \cdot N_x \cdot N_t}{t_{end} \cdot 10^6}.$$

where $N_x$ is number of lattices in x-axis direction, $N_y$ is number of lattices in y-axis direction, $N_t$ is number of iterations and $t_{end}$ is running time. Table 5 presents MLUPS for different graphics processing units when varying the grid size. Note that the results are given for 1000 iterations.

The data presented in Table 4 characterizes the computational TRT LB code as a memory-bound. Numerical performance of the GPU RTX 3080 with 8704 CUDA cores more than two times lower than Tesla V100 with 5120 CUDA cores. The peak performance for GTX 1060, RTX 3080 and Tesla T4 is found with the grid size of $4096^2$.

**Table 5.** Numerical performance.

| Grid | MLUPS | | | | | |
|---|---|---|---|---|---|---|
| | Tesla P100 | | Tesla T4 | | Tesla V100 | |
| | Float32 | Float64 | Float32 | Float64 | Float32 | Float64 |
| $1024^2$ | 557.75 | 348.36 | 338.25 | 74.42 | 1263.34 | 873.81 |
| $2048^2$ | 615.00 | 354.55 | 356.36 | 73.16 | 1677.72 | 1030.54 |
| $4096^2$ | 627.89 | 354.47 | 378.97 | 73.10 | 1749.45 | 1064.54 |
| $5632^2$ | 628.48 | 352.28 | 377.70 | 73.40 | 1776.00 | 1048.58 |

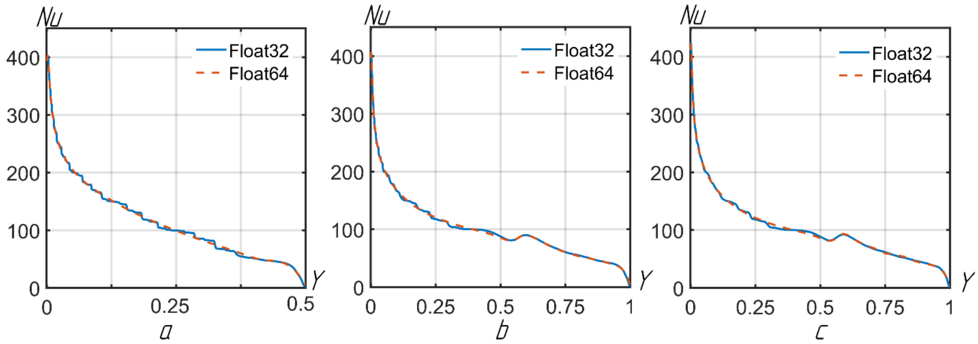


**Fig. 12.** Profiles of time-averaged local Nusselt numbers with $Ra$ = $10^{10}$ and Pr = 0.71, (a) $A_r$ = 0.5, (b) $A_r$ = 1, (c) $A_r$ = 2.

In contrast to the other hardware, the Tesla V100 maintains a slight speed-up as the mesh is refined. In general, the results indicate that the memory bandwidth is the dominant factor influencing computational performance. The GPUs with the GDDR memory type have a strong linear correlation between numerical performance and memory bandwidth. When utilizing the HBM2 memory type, numerical performance of the high-fidelity TRT LB model is significantly increased. In coarse-grid simulations without a turbulence model, the achieved performance of 1750 MLUPS is nearly sufficient for real-time prediction of heat and fluid flow patterns.

Figure 11 shows variation of time-averaged local Nusselt numbers at the hot wall. The Float32 denotes single precision variables whereas the Float64 is simulation using double precision variables.

Figure 12 indicates slight oscillations of local Nusselt numbers when using variables with single precision. Apparently, accumulation of round-off errors causes spurious currents which results in conserved quantities fluctuations. However, a comparison of single and double precision implementations revealed no significant discrepancy in outcomes for the tested parameters as shown in Table 3. Hence, the double precision variables are recommended for high-fidelity scientific computations whereas the double precision variables can be used for fast predictions in terms of engineering application.

## 4. Conclusion

A GPU-accelerated high-fidelity two-relaxation lattice Boltzmann solver combined with the direct explicit solution of energy equation is introduced. During numerical experiments, it was found that developed turbulent natural convection is characterized by the generation of multiple thermal plumes along the isothermal boundaries. This behavior cannot be predicted by the wide spread RANS models due to specific production of turbulent viscosity. When the cavity aspect ratio is higher than one, the core of the cavity remains stratified with $Ra = 10^{10}$ whereas fully curved isotherms shape is formed with $Ra = 10^{11}$. In the horizontal configuration, the development of thermal plumes is inhibited by the smaller length of the isothermal walls. This results in a uniform heat stratification when $Ra = 10^{10}$. However, vertical flow begins to dominate at $Ra = 10^{11}$ resulting in the formation of thermal plumes. In general, the time-averaged flow patterns are slightly affected by aspect ratio of the cavity. A global circulation pattern is established in which the inner currents are controlled by thermal plume dynamics. Distribution of the second order statistics is mainly determined by convective plumes dynamics. For the tall cavity configuration, the temperature variance and turbulent kinetic energy are significant along the vertical walls at a Rayleigh number of $10^{10}$. When increasing the Ra, $T_{var}$ and TKE migrate into the cavity core. On the contrary, the horizontal distribution of temperature variance and turbulent kinetic energy with $Ra = 10^{10}$ is altered to vertical distribution with $Ra = 10^{11}$ when $A_r = 2$. The reasonable extension of the present work is 3D problem formulation. However, for this case, multi-GPU approach should be considered since three-dimensional problem formulation drastically increases computational load. Along with that, high-fidelity simulation of conduction-convection-radiation coupling is of particular interest in terms of real practical applications.

## Author Contributions

All parts of the paper were written by A. Nee.

## Acknowledgments

Not applicable.

## Conflict of Interest

The author declares no potential conflicts of interest concerning the research, authorship, and publication of this article.

## Funding

The research was funded by the program of the National Research Tomsk Polytechnic University (Priority-2030-EEZTs-013-198-2025).

## Data Availability Statements

The datasets generated and/or analyzed during the current study are available from the corresponding author on a reasonable request.

## Nomenclature

| | |
|---|---|
| $a$ | Thermal diffusivity [m$^2$/s] |
| $c_k$ | Particle speeds [lu] |
| $c_s$ | Lattice speed of sound [lu] |
| $f$ | Distribution function [lu] |
| $f^{aeq}$ | Asymmetrical equilibrium distribution function [lu] |
| $f^{asym}$ | Asymmetrical distribution function [lu] |
| $f^{eq}$ | Equilibrium distribution function [lu] |
| $f^{seq}$ | Symmetrical equilibrium distribution function [lu] |
| $f^{sym}$ | Symmetrical distribution function [lu] |
| $g$ | Gravitational acceleration [m/s$^2$] |
| $L$ | Length of the cavity [m] |
| $Nu$ | Mean convective Nusselt number [-] |
| $Pr$ | Prandtl number [-] |
| $Ra$ | Rayleigh number [-] |
| $t$ | Time [s] |
| $t_0$ | Time scale [s] |
| $\Delta t$ | Lattice time step [lu] |
| $T$ | Temperature [K] |
| $T_c$ | Temperature of the cold wall [K] |
| $T_h$ | Temperature of the hot wall [K] |
| $u,v$ | Velocity components [m/s] |
| $U,V$ | Dimensionless analogies of $u$, $v$ [-] |
| $V_{nc}$ | Velocity scale [m/s] |
| $x,y$ | Cartesian coordinates [m] |
| $X,Y$ | Dimensionless analogies of $x$, $y$ [-] |
| $w_k$ | Weighting factor |

**Greek symbols**

| | |
|---|---|
| $\beta$ | Thermal expansion [1/K] |
| $\Theta$ | Dimensionless temperature [-] |
| $\nu$ | Kinematic viscosity [m/s$^2$] |
| $\rho$ | Density [kg/m$^3$] |
| $\tau$ | Dimensionless time [-] |
| $\tau_{asym}$ | Asymmetrical relaxation time [lu] |
| $\tau_{sym}$ | Symmetrical relaxation time [lu] |

## References

[1] Barakos, G., Mitsoulis, E., Natural convection flow in a square cavity revisited: Laminar and turbulent models with wall functions, *International Journal for Numerical Methods in Fluids*, 18, 1994, 727–739.
[2]. Chen, H.-T., Huang, Y.-C., Chen, K.-X., Chang, J.-R., Yan, W.-M., Experimental and numerical study of inverse natural convection-conduction problem in a fully partitioned cavity, *Numerical Heat Transfer, Part A: Applications*, 85, 2024, 4204–4227.
[3]. Chen, H.-T., Huang, Y.-C., Rashidi, S., Chen, K.-X., Yan, W.-M., Numerical and experimental studies on heat transfer characteristics and ventilation for indoor vertical farming system, *Thermal Science and Engineering Progress*, 52, 2024, 102667.
[4] Paolucci, S., Direct numerical simulation of two-dimensional turbulent natural convection in an enclosed cavity, *Journal of Fluid Mechanics*, 215, 1990, 229–262.
[5] Fusegi, T., Hyun, J.M., Kuwahara, K., Three-dimensional simulation of natural convection in a sidewall-heated cube, *International Journal for Numerical Methods in Fluids*, 13, 1991, 857–867.
[6] Trias, F.X., Gorobets, A., Soria, M., Oliva, A., Direct numerical simulation of a differentially heated cavity of aspect ratio 4 with Rayleigh numbers up to 1011 – Part I: Numerical methods and time-averaged flow, *International Journal of Heat and Mass Transfer*, 53, 2010, 665–673.
[7] Trias, F.X., Gorobets, A., Soria, M., Oliva, A., Direct numerical simulation of a differentially heated cavity of aspect ratio 4 with Rayleigh numbers up to 1011 – Part II: Heat transfer and flow dynamics, *International Journal of Heat and Mass Transfer*, 53, 2010, 674–683.
[8] Trias, F.X., Gorobets, A., Oliva, A., Pérez-Segarra, C.D., DNS and regularization modeling of a turbulent differentially heated cavity of aspect ratio 5, *International Journal of Heat and Mass Transfer*, 57, 2013, 171–182.
[9] Trias, F.X., Gorobets, A., Pérez-Segarra, C.D., Oliva, A., Numerical simulation of turbulence at lower costs: Regularization modeling, *Computers & Fluids*, 80, 2013, 251–259.
[10] Vasiliev, A., Sukhanovskii, A., Frick, P., Budnikov, A., Fomichev, V., Bolshukhin, M., Romanov, R., High Rayleigh number convection in a cubic cell with adiabatic sidewalls, *International Journal of Heat and Mass Transfer*, 102, 2016, 201–212.
[11] Sondak, D., Smith, T.M., Pawlowski, R.P., Condec, S., Shadid, J.N., High Rayleigh number variational multiscale large eddy simulations of Rayleigh-Bénard convection, *Mechanics Research Communications*, 109, 2020, 103614.
[12] Kizildag, D., Trias, F.X., Rodríguez, I., Oliva, A., Large eddy and direct numerical simulations of a turbulent water-filled differentially heated cavity of aspect ratio 5, *International Journal of Heat and Mass Transfer*, 77, 2014, 1084–1094.
[13] Dixit, H.N., Babu, V., Simulation of high Rayleigh number natural convection in a square cavity using the lattice Boltzmann method, *International Journal of Heat and Mass Transfer*, 49, 2006, 727–739.
[14] Sharma, K.V., Straka, R., Tavares, F.W., Natural convection heat transfer modeling by the cascaded thermal lattice Boltzmann method, *International Journal of Thermal Sciences*, 134, 2018, 552–564.
[15] Frapolli, N., Chikatamarla, S.S., Karlin, I.V., Entropic lattice Boltzmann simulation of thermal convective turbulence, *Computers & Fluids*, 175, 2018, 2–19.
[16] Wang, P., Zhang, Y., Guo, Z., Numerical study of three-dimensional natural convection in a cubical cavity at high Rayleigh numbers *International Journal of Heat and Mass Transfer*, 113, 2017, 217–228.
[17] Wen, X., Wang, L.-P., Guo, Z., Zhakebayev, D.B., Laminar to turbulent flow transition inside the boundary layer adjacent to isothermal wall of natural convection flow in a cubical cavity, *International Journal of Heat and Mass Transfer*, 167, 2021, 120822.
[18] Zhuo, C., Zhong, C., LES-based filter-matrix lattice Boltzmann model for simulating turbulent natural convection in a square cavity, *International Journal of Heat and Fluid Flow*, 42, 2013, 10–22.
[19] Chen, S., Liu, H., Zheng, C., Numerical study of turbulent double-diffusive natural convection in a square cavity by LES-based lattice Boltzmann model, *International Journal of Heat and Mass Transfer*, 55, 2012, 4862–4870.
[20] Lallemand, P., Lou, L.-S., Hybrid finite-difference thermal lattice Boltzmann equation, *International Journal of Modern Physics B*, 17, 2003, 41–47.
[21] Nee, A., Comparative Study of Hybrid Lattice Boltzmann and Vorticity-vector Potential Modelling of 2D and 3D Natural Convection Combined with Rosseland Radiation, *Journal of Applied and Computational Mechanics*, 8, 2022, 1467–1479.
[22] Nee, A., Hybrid Lattice Boltzmann Scheme for Conductive-convective-radiative Heat Transfer, *Journal of Applied and Computational Mechanics*, 11, 2025, 1149–1161.
[23] Nee, A., Evaluation of hybrid lattice Boltzmann models for laminar and turbulent natural convection, *International Communications in Heat and Mass Transfer*, 162, 2025, 108635.
[24] Ginzburg, I., Verhaeghe, F., d'Humieres, D., Two-relaxation-time lattice Boltzmann scheme: About parameterization, velocity, pressure and mixed boundary conditions, *Communications in Computational Physics*, 3, 2008, 427–478.
[25] Feng, Y.-L., Guo, S.-L., Tao, W.-Q., Sagaut, P., Regularized thermal lattice Boltzmann method for natural convection with large temperature differences, *International Journal of Heat and Mass Transfer*, 125, 2018, 1379–1391.

[26] Ampofo, F., Karayiannis, T.G., Experimental benchmark data for turbulent natural convection in an air filled square cavity, *International Journal of Heat and Mass Transfer*, 46, 2003, 3551–3572.
[27] Kerr, R.M., Rayleigh number scaling in numerical convection, *Journal of Fluid Mechanics*, 310, 1996, 139–179.
[28] Trias, F.X., Soria, M., Oliva, A., Pérez-Segarra, C.D., Direct numerical simulations of two- and three-dimensional turbulent natural convection flows in a differentially heated cavity of aspect ratio 4, *Journal of Fluid Mechanics*, 586, 2007, 259–293.
[29] https://julialang.org/
[30] https://github.com/omlins/ParallelStencil.jl

## ORCID iD

Alexander Nee https://orcid.org/0000-0002-7928-0329



**How to cite this article:** Nee A. GPU-Accelerated High-Fidelity Simulation of Turbulent Natural Convection, *J. Appl. Comput. Mech.*, 12(3), 2026, 1276-1287. https://doi.org/10.22055/jacm.2026.48841.5540